OPEN ACCESS



Magnetic Fields Observed along the East–West Outflow of IRAS 16293-2422

Frankie J.Encalada, Leslie W. Looney, Giles Novak, Sarah Sadavo, Erin G. Cox, Fabio Pereira-Santo, Dennis Lee^{3,4}, Rachel Harrison⁷, and Kate Pattle⁶ Department of AstronomyUniversity of Illinois, 1002 West Green StUrbana, IL 61801, USA; fje2@illinois.edu

²National Radio Astronomy Observator<u>\$</u>20 Edgemont Rd.Charlottesville,VA 22903, USA ³ Center for Interdisciplinary Exploration and Research in Astronomy (CIERM)rthwestern University1800 Sherman Ave Evanston, IL 60201, USA Department of Physics & Astronomylorthwestern University2145 Sheridan Rd Evanston, IL 60208, USA

5 Department for PhysicsEngineering Physics and Astrophysicaueen's UniversityKingston,ON K7L 3N6, Canada Max Planck Institute for AstronomyKönigstuhl 17,69117 HeidelbergGermany ⁷ School of Physics and Astronom Monash University Clayton VIC 3800, Australia ⁸ Department of Physics and Astronomyniversity College LondonGower St.,London WC1E 6BT,UK Received 2024 February 19; revised 2024 May 4; accepted 2024 May 7; published 2024 June 17

Abstract

Magnetic fields likely play an important role in the formation of young protostars. Multiscale and multiwavelength dust polarization observations can reveal the inferred magnetic field from scales of the cloud to core to protostar. We present continuum polarization observations of the young protostellartriple system IRAS 16293-2422 at 89 µm using HAWC+ on SOFIA. The inferred magnetic field is very uniform with an average field angle of 89° ± 23° (E of N), which is different from the ~170° field morphology seen at 850 µm at larger scales (□2000 au) with JCMT POL-2 and at 1.3 mm on smaller scales (□300 au) with Atacama Large Millimeter/submillimeter Array. The HAWC+ magnetic field direction is aligned with the known E-W outflow. This alignment difference suggests that the shorter wavelength HAWC+ data is tracing the magnetic field associated with warmer dust likely from the outflow cavity, whereas the longer wavelength data are tracing the bulk magnetic field from cooler dust. Also, we show in this source the dust emission peak is strongly affected by the observing waveleting that continuum peaks closer to source B (northern source) at shorter wavelengths and progressively moves toward the southern A source with increasing wavelength (from 22 to 850 µm).

Unified Astronomy Thesaurus concepts: Young stellar objects (1834)

1. Introduction

star formation processon all scales, from the assembly of et al. 2023; Tsukamoto et al. 2023). Nevertheless, the details of the protostars exhibiB-fields that are perpendicular to the molecular cloud structure to protostellar accretion (eRattle how magnetic fields affect star formation are not well observationally constrained magnetic field is difficult to directly observe in most regions. he most common approach is to use dust polarization emission to infer the plane-of-the-sky and/or evolution of binaries and multiple systems. Mainmagnetic field orientation. This is possible due to radiative alignment torques that tend to align the short axis of elongated stellar mass: the mean frequency of stellar companions per dust grains with the magnetic field (e.g., Lazarian 2007). As a direction that is perpendicular to the field. Many studies therefore rotate the polarization angles by 90° to presethte inferred plane-of-sky magnetic field morphology. Although this technique works very well in most star-forming regions and spatial scales when resolving the circumstellar disk other polarization mechanisms such as scattering dominate (e.g., Kataoka et al. 2015; Yang et al. 2016; Cox et al. 2018; Harris et al. 2018; Sadavoy et al. 2019). This makes it very difficult to tation by gravitational instability and turbulentfragmentation measure the magnetic field morphology on smadales using dust polarization observations.

On the other hand, there have been a few surveys of the magnetic field in the inner envelope of protostars comparing the average B-field axis with the outflow axis (Hull et al. 2014;

Original content from this work may be used under the terms of the Creative Commons Attribution 4.0 licence. Any further distribution of this work must maintain attribution to the author(s) and the title of the work, journal citation and DOI.

Zhang et al. 2014; Galametz et al. 2018). Most recently, Huang Magnetic fields are thought to be a critical component of the et al. (2024) surveyed 61 protostars in Orion (with 56 detections) from the Class 0/I identified disk sources in the VANDAM survey (Tobin et al. 2022). They found that ~40% source outflows on scales of 400–1000 au, with the remainder of the sources being consistent with random alignment.

The magnetic field may also play a role in the formation sequence stars exhibite multiplicity rate that increases with primary rises from 0.5 for solar-type main-sequence stars to 2.1 result, the thermal emission of dust grains will be polarized in a for O-type main sequence primaries (Moe & Di Stefano 2017).

In addition, the multiplicity fraction is larges in the youngest populations of protostars (Tobin etal. 2016; Encalada etal. 2021; Tobin et al. 2022), likely decreasing as the systems age. To better understand binary formationwe must observe the youngest protobinary systems during binary formation. For young binary systems with separations <500 au, we expect the formation pathways are likely a combination of disk fragmenwith migration, whereas in systems with separations >1000 au the binary formation mechanism is likely dominated by turbulent fragmentation (e.g. Adams et al. 1989; Padoan & Nordlund 2002; Moe & Kratter 2018; Lee et a2019).

> IRAS 16293-2422 is a well-studied Class 0 protostellar triple system located in the p-Ophiuchi star-forming region inside the dark cloud L1689N (Lynds 1962) at a distance of 141 pc (Dzib et al. 2018). The IRAS 16293 system consists of two close binaries in the southeast (separated by 54 au), sources A1 and A2, (Wootten 1989; Maureira et al. 2020), and a single

protostarin the northwest, source B (separated by 725 au; Wootten 1989; Looney et al. 2000). SourcesA and B are embedded in a large (6 – 8×10³ au) envelope (e.g.Schöier et al. 2002; Crimier et al. 2010) with a bridge of material connecting them (e.g., Looney et al. 2000; Pineda et al. 2012). PID 07_0147 (PI: Novak). The bandwidth was 16.9 µmthe Although there had been speculation that source B was a more angular resolution (fullwidth at half maximum; FWHM) was evolved T Tauri star (Stark et al. 2004), observations of an inverse P-Cygniinfall profile toward source B (Pineda et al. 2012) indicate that the differences in the sources are more due to viewing angle, as source B is likely face-on (e.g., Rodríguezbroadband filters for continuum, a rotating half-wave plate that et al. 2005) whereas the binary sources A1 and A2 are more edge-on (Pineda et a2012).

With three protostars and their geometry, the system has both complicated envelope and outflow structures. The envelope has complex chemistry (e.glørgensen et al. 2016), and due to the multiplicity and the connecting bridge, the envelope presents difficulties in modeling the source details (Jacobsen et al. 2018). The system has large and impressive outflows that even at their discovery were known to be multilobed and very complicated, likely due to multiple systems(e.g., Fukui et al. 1986; Wootten & Loren 1987; Walker et al. 1988; Mizuno et al. 1990). The multiple outflows, some of which are observed only on large scales while others are observed only on small scales, are well summarized in vandata reduction pipeline, which produces science-ready conder Wiel et al. (2019) and many references within.

On the largest scaleshere are two observed outflows: east (blue)-west(red) (Fukui et al. 1986; Wootten & Loren 1987; Walker et al. 1988; Mizuno et al. 1990; Stark et al. 2004) and northeast(red)-southwes(blue) (Walker et al. 1988; Mizuno et al. 1990; Stark et al. 2004). However atsmaller scales the northeast-southwest outflow is not detected plying that the launching engine was quenched (van der Wiel et al. 2019). Or the other hand, the east-westoutflow, which is driven by source A, is clearly detected on smaller scales with interferometers (Yeh etal. 2008; Girart et al. 2014; van der Wiel et al. 2019). An additional outflow detected only on the small scale is aligned northwest(blue)-southeas(red) originating slightly north of source A with a blue bowshock in the location of source B (Kristensen et al. 2013; Girart et al. 2014). result for that pixel. If the χ^2 is larger, then we inflate the Although there are some observational hints of an outflow from pipeline error (also see Novak 2011;Chapman etal. 2013). of source B (Kristensen et al. 2013; Girart et al. 2014). source B (e.g., Yeh et al. 2008), there are no observations that Following Cox et al. (2022), we perform the inflation by fitting show clear evidence of outflow emission from source B.

In this paper, we present far-infrared observations (89 µm) on the scale of ~1000 au toward IRAS 16293-2422. The observationsused the High-Resolution Airborne Wide-band Camera (HAWC+; Vaillancourt et al. 2007; Harper et al. 2018) on board the Stratospheric Observatory Fornfrared Astronomy (SOFIA). We use the 89 µm dust continuum observations (Clarke et al.2020) by to infer the magnetic field in the envelope of IRAS 16293-2422, hereafter called IRAS 16293. The inferred magnetic field morphology is compared to 850 µm observation from the POL-2 polarimeter on the James Clerk Maxwell Telescope (JCMT) and to 1.3 mm observations from the Atacama Large Millimeter/submillimeter Array (ALMA). In addition, we compare the peak flux location variation with wavelength using archival observations from Wide-field Infrared Survey Explorer (WISE), Herschel, and SCUBA 2 on the JCMT.

The paper is organized as follows Section 2 we present the observations and data reduction. Section 3 covers the Section 5 contains our conclusions.

Observations and Data Reduction

We observed IRAS 16293 on 2019 July 23, between 12:21:13 and 12:25:41 UTC, using HAWC+ at Band C (89 µm). The observations were part the Cycle 7 program 7."8, and the field of view for the total intensity and polarimetry was 4.2×2.7 and 2.1×2.7 , respectively.

The HAWC+ instrument is a far-infrared detector with five modulates the incoming polarization and a grid that orthogonally separates the polarization ultiple cycles of standard nodding and chopping were used to build an image within a few minutes (Hildebrand et al. 2000). The instrument typically nods at 0.1 Hz and chops at 10 Hz. The four dithered positional observations are used to construatsingle imaging block or dither set. Due to a lack of bright visual guide stars in the region, there was a small offset in some of the imaging blocks. To correct this, we shifted the fit map Gaussian peak center to align with the archival map from Herschel's Photodetector Array Camera & Spectrometer (PACS) at 100 µm. No individual observation was offset by more than half a beam.

The raw images are then processed through the HAWC+ tinuum and polarization products. The details of the process are summarized in Harper et al. (2018). Briefly, the pipeline flatfields the demodulated and usable chopped data, calculates the Stokes I, Q, and U parameters from the combined nodded fluxes, and then corrects the pointing and instrumental polarization. Calibrations are applied to the flux via standard atmospheric opacity models using Neptune planetary observations. Finally, the Stokes maps are combined via standard regridding and Gaussian smoothing (Houde & Vaillancourt 2007). We smoothed the final maps to increase the signal-to-noise in the lower surface brightness regions away from the central source reating a final beam size of 1/7.

We compared our Stokes I, Q, and U maps across the different dither sets using a² χ analysis. A χ^2 is calculated for each pixel, which is then compared with the pipeline error a parameterized $\hat{\chi}$ with Stokes I intensity, allowing us to inflate each pixel based on its continuum brightness. This was done to handle the uncertainties more carefully in the brightest regions, where intensity-dependent errors dominate.

Finally, the percent polarization (p) and its error (σ_p) are calculated for each pixel following the HAWC+ handbook

$$P = 100\sqrt{\left(\frac{Q}{I}\right)^2 + \left(\frac{U}{I}\right)^2} \tag{1}$$

$$s_{p} = \frac{100}{I} \sqrt{\frac{\frac{1}{(Q^{2} + U^{2})}(Qs_{Q}^{2} + Us_{U}^{2} + 2QUs_{QU})}{+\left[\left(\frac{Q}{I}\right)^{2} + \left(\frac{U}{I}\right)^{2}\right]s_{I}^{2} - 2\frac{Q}{I}s_{QI} - 2\frac{U}{I}s_{UI}}}, (2)$$

results of the observations. Section 4 discusses the results, and here φ_0 and φ_1 are the uncertainties in Stokes Q and U and where $\sigma_{\!\!\! QU}, \; \sigma_{\!\!\! QI}, \;$ and $\sigma_{\!\!\! UI}$ are the covariance uncertainty terms. The polarization fraction is debiased following the HAWC+ handbook (Clarke et al. 2020) by = $\sqrt{p^2 - s_p^2}$. From all of these, the debiased polarization interestry ($I - p_{c}/100$) and its errors are calculated. Although the uncertainties are calculate per pixel, the median Stokes I rms is σ 2.2 mJy arse \tilde{c} , and the median polarization intensity rms=0.22 mJy arse \tilde{c} .

For the final maps, we selected the debiased polarization vectors that met the criteria of $P \psi \sigma_p > 3$, the debiased polarization percentage was 50%, and the Stokes I flux values were atleast × 10 the Stokes I rms noise level. While this was done at every pixel in the image, we present only enough vectors to be considered Nyquist sampled, for a total of 45 polarization vectors.

We estimate the overallflux calibration uncertainty of the observations a20%, but for the remainder of the paperany flux uncertainty listed will only be considered statistical uncertainty.

2.1. Archival Data

To compare our polarization observations with other wavelengths, we used JCMT POL-2 850 µm wavelength polarization observations at 4" resolution from Pattle et al. (2021), and ALMA Band 6 (1.3 mm wavelength) polarization observations from (Sadavoy et al. 2018), smoothed to 1" resolution.

In addition, we also used Herschel70, 100, and 160 μ m PACS data and 250, 350, and 500 μ m Spectral and Photometric Imaging Receiver (SPIRE) data.

We included the 24 µm Spitzer Multiband Imaging Photometer (MIPS) data. All of these data were obtained from the HerschelScience Archive. Lastly, the 22 µm WISE data from the NASA/IPAC Infrared Science Archive. were also included.

3. Results

Figure 1 shows the HAWC+ Band C (89 μ m) dust continuum observationsof IRAS 16293 with the inferred magnetic field polarization direction (i.e.polarization rotated by 90°) plotted over the 89 μ m continuum map as line segmentshereafter called vectors.

We fit the protostellar envelope continuum emission using a Gaussian. The protostellar envelope is resolved with a deconvolved fit size of 10.73 ± 0.74 by 8.7 ± 0.4 with a position angle (PA) of $10.8^{\circ}\pm11^{\circ}$. The integrated fit flux is 1236 ± 25 Jy and the peak flux is 1.25 ± 0.02 Jy arcsec

The continuum Gaussian fit of the HAWC+ 89 μ m observation is different than Gaussian fits to the Herschel archival data. The PACS 100 μ m source fits are somewhat smaller (7!7±0 \pm by 4 8 \pm 0 4 \pm and a PA of 141° \pm 5°), whereas the PACS 70 μ m source fits are a little larger (*11 9 \pm 0 \pm 0 \pm 0 3 and a PA of 113° \pm 7°). The variation indicated in the Gaussian fits of the HAWC+ and PACS 70 and 100 μ m images likely arises from differences in the

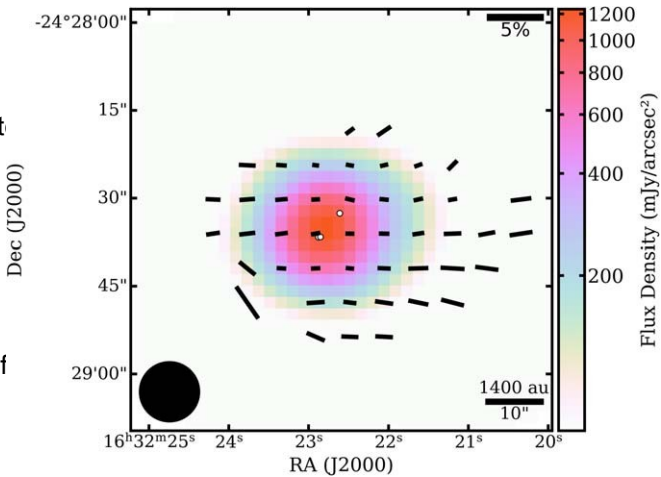


Figure 1. HAWC+ 89 μ m continuum map overlaid with the inferred magnetic field direction in black. The three protostellar peaks at 3 mm are shown in white (Maureira et al.2020), source A1/A2 in the south and source B in the north. The vectors were selected to show Nyquist sampling. The image has a smoothed image beam size of 1/7. The polarization scale bar is in the top right corner, the beam is in the bottom left corner, and a spatial scalebar of 10 (1400 au) is provided in the bottom right corner.

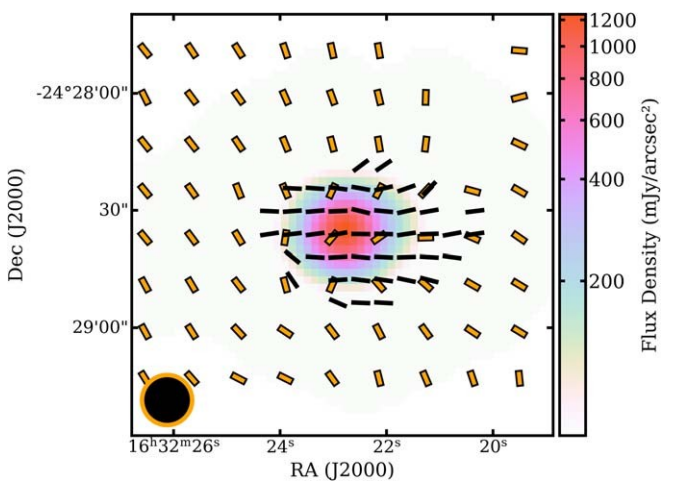


Figure 2. Our continuum map overlaid with our normalized, Nyquist sampled inferred magnetic field vectors in black. In orange vectors, we show the 850 µm POL-2 normalized vectors from Pattle ed. (2021) at the published pixel scale of 12 The corresponding beams. "11 7 and 14" for our observation and POL-2, respectively are in the bottom left corner.

source morphologies (e.g., outflows, envelopes, and the bridge connecting source A and B) so close to the overall emission peak near 100 $\mu n On$ the other hand,the PA from the HAWC+ Band C fit is within 10° of the 850 μm dust emission (Pattle et al. 2021), although the 850 μm core extension is measured on much larger scales.

We can compare the inferred magnetic field from other observations with varying wavelength and spatial scales. Figure 2 shows the inferred magnetic field from our 89 µm data from Figure 1 (black vectors) with the 850 µm data from POL-2 (orange vectors) which have 14" resolution and 12" pixels (Pattle et al. 2021), both wavelengths presented as normalized vectors. The vectors align on the western side of the source (and one vector in the southeast), but otherwise, there is generally notmuch agreement the inferred magnetic field direction.

⁹ PACS observing labels 1342205093, 1342205094, 1342227150, and 1342227151.

¹⁰ SPIRE observing labels 1342205093 and 1342205094.

¹¹ MIPS observing label 4321536.

¹² http://archive.esac.esa.int/hsa/whsa/

¹³ WISE observing coadd id: 2477m243_ac51.

¹⁴ https://irsa.ipac.caltech.edu/applications/wise/

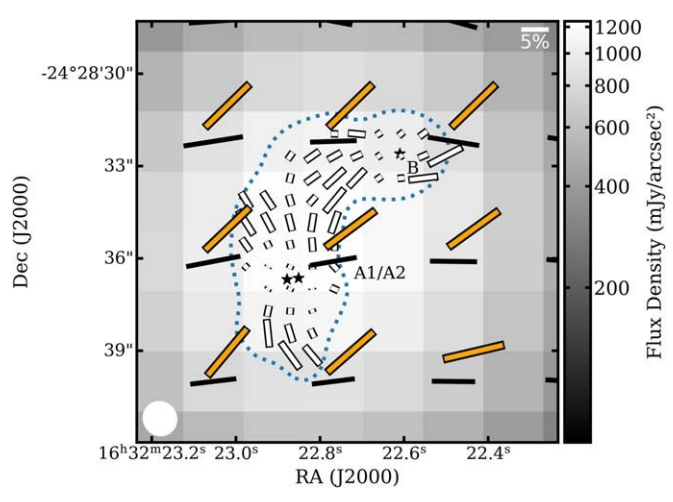


Figure 3. The HAWC+ 89 μm continuum image overlaid with the normalized magnetic field vectors from HAWC+ in black and from POL-2 in orange. Both maps show oversampled vectors at 4" pixels to better match the ALMA scales is our HAWC+ Stokes I map. From right to left: the magenta marker is the The white vectors show the ALMA 1.3 mm polarization vectors, smoothed to 1" resolution (white beam in the bottom left corner). The ALMA vectors are not normalized, and a 5% scale bar is given in the top rightorner. The dotted contourshows the ALMA continuum at the 10 σ level, where σ = 1.72 mJy arcsec¹. The locations of the hierarchicatriple protostars (source A1/A2 and source B) at 3 mm (e.g., Maureira et al. 2020) are labeled The bridge is the region connecting the two sources.

On the other hand, misalignment is also seen when comparing the core scale (POL-2) with the cloud scale (Planck). As pointed out by Pattle et al. (2021), there is a misalignmentof the large-scale Planck field with the POL-2 850 µm magnetic field near the IRAS 16293 protostars, which is also seen in Figure 2 as a field shift near the protostars compared to the outer region. In Figure 1, the inferred HAWC+ magnetic field is generally aligned E-W. This is offset by ~65° from the overall ~arcminute large-scale field inferred from Planck observations of the Ophiuchus L1689 molecular cloud corewhich is 24°E of N (Pattle et al 2021).

At a higher spatial scale, Figure 3 compares the 89 µm HAWC+ data and 850 µm POL-2 data with high-resolution polarization observations at 1.3 mm with ALMA from Sadavoy et al. (2018), which are consistent with 880 µm polarization observations from Rao etal. (2009). The ALMA data have been smoothed to 1" resolution to bettercompare with our observations.

Note that the region mapped in Figure 3 is only slightly larger than the POL-2 and HAWC+ beam sizes, so it is difficult to do more than compare broadly. However, in general, the vectors from the three observations are notellaligned. The HAWC+ and ALMA observations have some agreementto the northwest, and the ALMA and POL-2 observationshave some agreementin the bridge region between source A and B.On the other hand, HAWC+ and ALMA observations are antialigned in the south, while ALMA and POL-2 observations are antialigned in the middle-eastern side.

4. Discussion

4.1. Continuum Wavelength Dependence

When comparing the HAWC+ dust continuum emission Gaussian fits with the Gaussian fits from Herschest, well as

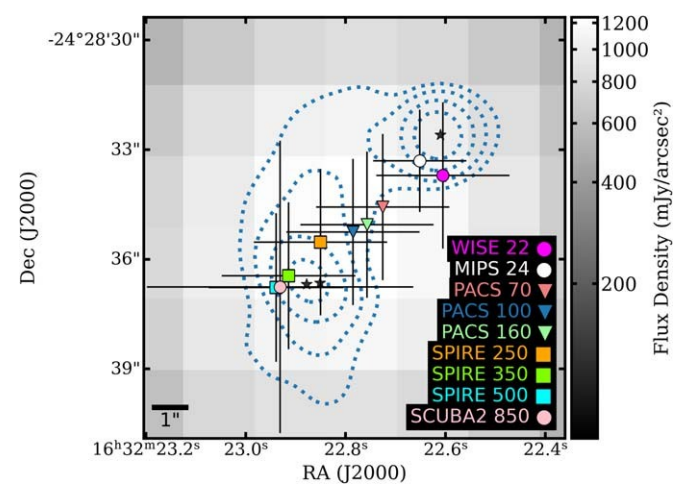


Figure 4. Image of the IRAS 16293-2422 system with Gaussian-fitpeak positions observed by various telescopes/instrume Titre background image Gaussian peak of the WISE W4 filter a22 µm; the white marker is Spitzer MIPS 24 µm peak; light coral, pale green, and blue corresponding to Herschel PACS at 70, 160, and 100 μm orange and chartreuse for SPIRE 250 and 350 μm ; the pink marker corresponding to SCUBA-2 at 850 μm ; and the cyan is SPIRE at 500 µm. Errors represent pointing uncertainties collected from the respective telescope's manualain publications or relevantsources (WISE; Wright et al. 2010), MIPS on Spitzer (MIPS Instrument And MIPS Instrument Support Teams 2011), PACS & SPIRE on Herschel (Sánchez-Porta& Marston et al. 2014), SCUBA2 on JCMT (Pattle et al. 2015; Kirk et al. 2018). Contours are 1.3 mm continuum from ALMA (smoothed to) with levels at N σ for N ä [10, 30, 100, 300] and σ = 1.72 mJy arcsec et al. 2018).

the emission varied with wavelength, with the far-infrared wavelengths peaking between the protostellar source locations. As expected, the flux peak dust continuum of the IRAS 16293-2422 system is strongly dependent on observing wavelength, as can be seen in the spectralenergy distribution from Schöier et al. (2002) with a maximum around 100 µm, but it also seems that the spatial location of the peak is very strongly dependent on observing wavelengthBy using the archivalobservations, we can compare this trend more broadly.

We fit the different wavelength emissions(e.g., WISE, Herschel, and SCUBA2 listed in Section 2) to Gaussians. Figure 4 shows the Gaussian fit peak to wavelengths from 22 to 850 µm. There is a clear gradient from northwest to southeast from short wavelengths to long wavelengths other words, we detect a gradient in the cloud dust temperatureswith wavelength. This is likely due to differences in the morphology or detailed properties of the source ossibly arising from the structure of the envelope or disks in the binary system.

Another explanation for the shiftn wavelength could be a difference in the evolutionary stage of the binary sources stated in Section 1, source B has been argued to be more evolved than source A (Stark et al. 2004). As we probe shorter and shorter wavelengths, we are most sensitive to the hot dust in the less obscured source lowever, the evolutionary stages of the protostars are still uncertain with most recent work suggesting that the sources are likely at about the same evolutionary stage or that source B is slightly less evolved (van der Wiel et al. 2019), but the evolutionary ages are still a point of contention.

One of the complications is that the two protostars have different inclinations with respect to the line of sight. Source A, the peak in the POL-2 observations, we noted that the peak of which is the tight binary, is closer to edge-on (inclinations of

59° and 74°; Maureira et al. 2020) while source B is close to face-on (inclination ~18°;Zamponi et al. 2021). The source A protostars are modtkely Class 0 based on evidence of them of source B is harder to verify due to its face-on inclination and lack of outflow activity (see, Yeh et al. 2008). The difference in sould explain the observed peak shifteen atthe driving active outflows (e.g., Yeh et al. 2008), but the evolution sensitive to the hotter dust seen in the more face-on disk, which is less obscured. In addition, source A is also surrounded by a ~100 au circumbinary disk with a PA of ~50° (Maureira et al. 2020), which could increase the obscuration for the binary. We suggest that such continuum peak positional shifts with wavelength may be present other binary sources requiring careful consideration of variation in peak position at the shorter wavelengths.

1200 -24°28'00' 1000 800 15 600 Flux Density (mJy/arcsec² 30 45 29'00 1400 au 10' 16h32m25s 24s 23^s 225 21 20 RA (J2000)

Figure 5. Same as Figure 1 but overlaid with the blue and red ¹²CO 3–2 outflow contour lines of Yeh et al. (2008) using contours at 3σ , 10σ , 30σ , and 50σ , where σ is 1.4 Jy beam for the blue and 2.3 Jy beam for the red.

4.2. Magnetic Fields

At the large scales in dense, elongated structures or filaments of molecular clouds, the magnetic field's alignment depends on nave a very different measured polarization angle 9° ± 23°, column density below a critical column density the magnetic field is preferentially oriented parallelto the elongation of density structures, and above, the magnetic field is preferentially ap is the uniform field that is nearly completely E-W in perpendicular (Planck Collaboration et 20.16). However, the details of the alignment may vary across star formation regionsplanck-, JCMT-, and ALMA-inferred magnetic field angles. (Stephens et al. 2022). Using HAWC+ observations in L1688, iAlthough one could argue for large field morphological has been shown that the transition occurs at a molecular hydrogen column density of $\sim 10^{1.7}$ cm⁻² (Lee et al. 2021). Magnetohydrodynamicsimulations have suggested that the transition may coincide with the kinetic energy of the gravitationally induced flows surpassing the magnetic energy (Chen et al. 2016).

One of the goals of our observations was to compare the inferred magnetic field in the far-infrared dustcontinuum to other resolutions and scales that impact the star formation process. The large-scale Planck-inferred magnetic field in the L1689-N region is 24°E of N (Pattle et al. 2021), i.e., nearly perpendicular to the large L1689/L1712 filament identified in Ladjelate et al. (2020). These large-scale Planck fieldsare generally consisten with the 850 µm JCMT POL-2 inferred core (e.g., see Figure 4 in Pattle et al. 2021). This is not surprising as the overal Planck field seems to exhibit small shift at the core that suggests unresolved morphology.

When one traces the magnetic field from the L1689-N core scale down to the protostellarenvelope scale with the three observations in Figure 3, we see regions where the inferred magnetic fields are aligned but other regions where the inferred 2008). Our magnetic field vectors are wellaligned with this magnetic fields are misaligned. The HAWC+ and ALMA observations are aligned in the northwest, while the ALMA andmore in the southNonethelesspased on this comparisonwe POL-2 observations are well aligned in the bridge region between source A and B.On the other hand, HAWC+ and ALMA observations are misaligned in the south, while ALMA and POL-2 observations are misaligned on the eastern side. However, as pointed outby Pattle et al. (2021), the average field angles are consistent between ALMA and POL-2: 166° ± 31° for POL-2 at the cloud core and 176° ± 54° and 130° ± 14° averaged around the protostars only and the bridgefields perpendicular to the source outflow. between them only in the unsmoothed ALMA data in Sadavoy

which is more in line with the E-W outflow.

Indeed, one of the most striking features of the HAWC+ direction, which is very different morphologically to the connections or trends between the mapped fields in Figure 3, there is still no overall coherence across wavelengths. The key to understanding these different wavelength observations is that the observations are probing differentical depths and dust temperatures (as seen clearly in Figure 3), making it difficult to piece together the overall 3D magnetic field morphology without a better understanding of the system details.

The IRAS 16293-2422 triple system has a complicated morphology with the protostars disks, a bridge feature, and multiple outflows observed on different spatial scales (see Figure 1 in van der Wiel et al. 2019). To date, the outflows have only been associated with source A, which is likely due to the face-on inclination of source B or possibly a difference in the evolutionary stage. As discussed in Section 1, source A has magnetic fields shown in Figure 2, although in detail the POL-2two outflows on the thousands of au scale: one east-west (e.g., fields are less aligned with the overall Planck field at the cloud Yeh et al. 2008) and one northwest-southeast (e.g., Kristensen et al. 2013). Arguably, the east-westoutflow dominates the system on the cloud core scale (e.g., Mizuno et al. 1990; Stark et al. 2004), which is also well detected in higher resolution interferometric observations (Yeh et 2008). Figure 5 shows our inferred magnetic fields with the blue- and redshifted outflows as identified from CO (3-2) observations of Yeh et al. outflow direction, with the exception of our vectors extending posit that the HAWC+ observations are tracing the warm dust from the E-W outflow cavity or cavity walls of IRAS 16293-2422 (Stark et al. 2004). This is in contrast to the average magnetic field from the POL-2 and ALMA observations, which are approximately perpendicular to the E-W outflowOn the other hand, this is consistentwith the Huang et al. (2024) survey, where ~40% of the sources have average magnetic

There are many morphological examples of the outflows of et al. (2018), respectively. Whereas the HAWC+ observations protostars seeming to modify or shape the magnetic field of the core as traced by single-dish observation@rion A filament (Pattle et al. 2017), NGC 2071IR in Orion B (Lyo et al. 2021), mean an average field of 179° ± 23°, which is closer to the and CB 54 (Pattle et al. 2022), or to modify or shape the inner bulk average magnetic fieldsof 166° ± 31° for POL-2 and protostellar envelope as traced by interferometric observations:176° ± 54° for ALMA data, in detail the vectors in the inner Serpens SMM1 (Hullet al. 2017), B335 (Maury et al. 2018), Emb 8(N) (Le Gouellec et al2019), and BHR 71 IRS2 (Hull et al. 2020).

Additionally, the short wavelength observational-inferred magnetic field can exhibit different morphologies compared to is commonly detected in magnetic-field-aligned dustgrain the longer wavelengths Orion, for example, the HAWC+ shorter wavelengths (53 and 89 µm compared to 154 and 214 µm) are more aligned with the bipolar outflow structure in the BecklinNeugebauer/KleinmanLow regionas traced by molecular tracers (Chuss et 2019). The longer wavelengths are argued to be tracing the cooler duthat is outside of the explosion-influenced region.

In this case for IRAS 16293-2422, the 89 µm continuum emission is tracing the warmer dusturrounding the outflow. The magnetic field morphology in this region is dominated by the outflow and not the magnetic field in the cloud core or the bridge, which is seen to dominate at longer wavelengt his is somewhatconsistentwith the continuum peak of IRAS 16293-2442 at ~100 µm being near the center of the system so We present the 89 µm continuum polarization emission that the polarization is dominated by the large opening angle cavity seen in Figure 5.

4.3. Possibility of Polarization by Dichroic Extinction

As the inferred magnetic direction in Figure1 is different than what is observed at 850 µm with POL-24e should also examine other polarization mechanisms thatay account for the observations. The most likely other polarization mechanism would be dichroic extinction, used in the optical or infrared to infer magnetic fields from polarization observations oftars extinct by aligned dust grains (e.g., Scarrott & Warren-Smith 1989). Although dichroic extinction depends on dust properties optical depth, and temperature gradients (also see Hildebrand et al. 2000), we can consider the effect in the typical case for young stellar objects when unpolarized, or weakly polarized, emission is extinct by cooler foreground dust that has its grains aligned by magnetic fields or other means. In that case, the dust grain's long axis will have more efficient extinction than the shortaxis, so the light is now polarized along the dust's short axis, which would result in a 90° flip in the polarization compared to the inferred magnetic field from the emission of aligned dust grains. The effect has been seen in far-infrared dustpolarization observationsparticularly in the Sagittarius B2 molecularcloud (Dowell 1997; Novak et al. 1997). The process will be most effective in optically thick sources with a temperature gradient.

Although, we can not rule out dichroic extinction as the dominant mechanism for polarization in IRAS 16293-2422 (seeshould include multiwavelength observationsthat sample Zielinski et al. 2021, where they argue that dichroic extinction multiple scales and all the structures of star formation. polarization is not important in HAWC+ observations of B335), there are a few reasons to disfavorthat explanation. First, we do not see a strong signature of the 90° flip toward the outside of the source, as is seen, for example, in observations of Based on observations add with the NASA/DLR Strato-NGC 1333 IRAS4 (Ko et al. 2020) and OMC-3/MMS 6 (Liu 2021). In fact, with the exception of two vectors, Figure 1 shows a very uniform inferred magnetic field. Of course, such anc. (USRA), under NASA contract NNA17BF53C, and the flip is not necessarybut if we flip all of our vectors by 90°, then the vectors on the westn Figure 2 that currently agree with the POL-2 and ALMA vectors would disagreeSecond,

although a flip of 90° for the inferred magnetic field would region of the source, see Figure 3 for example, would not better match with a HAWC+ flip of 90°. Third, the polarization fraction is lower toward the center of our observationsin Figure 1. Such polarization depression with increasing density polarization observations (e.gChuss et al. 2019) and is not seen in regions where the polarization is due to dichroic extinction (Dowell 1997: Novak et al. 1997: Ko et al. 2020). Finally, east-westmagnetic fields have also been detected along a few stellar sight lines in the L1689 cloud at optical wavelengths (e.g.Vrba et al. 1976), suggesting that there are east-west fields in some parts of the region. Overall, based on these four reasons, the IRAS 16293-2422 polarization observations presented here are most likely due to the magnetic field alignment of dust grains.

5. Conclusions

toward the protostellar system IRAS 16293-2422 using the HAWC+ polarimeter onboard SOFIA. Our main conclusions are:

- 1. We detect a uniform magnetic field in the inner region of IRAS 16293-2422 that is aligned east-west. The average field angle in the HAWC+ observations is 89° ± 23°, which is consistent with one of the known large-scale outflows. This is different from the average field angles at longer wavelengths: Planck large-scaleaverage field angle of 24°, JCMT POL-2 average field angle of 166° ± 31°, and the ALMA average field angle near the protostars of 176° ± 54°.
- 2. We posit that the magnetic field probed by the 89 µm continuum emission is dominated by the outflow magnetic field, while the 850 µm dust emission is dominated more by the core magnetic field.
- 3. The continuum peak of the source varies significantly with wavelength, moving from near source B at the mid-IR to near source A in the far-IR. This is either a consequence of the evolutionary state of the two sources or more likely due to the difference in inclination. The shorter wavelengths are more sensitive to the warmer dust, which is seen in source B.

These observations suggesthat magnetic fields in young protostarsare likely more complicated than simple pictures suggest with multiple field morphologies dominating at various scales and in different structures. Any observational constraints

Acknowledgments

spheric Observatory for Infrared Astronomy (SOBOFIA is jointly operated by the Universities Space Research Association, Deutsches SOFIA Institut (DSI) under DLR contract 50 OK 0901 to the University of Stuttgart.L.W.L. acknowledgesupport from NSF AST-1910364 and NSF AST-2307844.R.E.H.

acknowledges support from NSF AST-19103641. is grateful Kataoka, A., Muto, T., Momose, M., et al. 2015, ApJ, 809, 78 for NASA support for this work, via award Nos. SOF 06-0116 aNd, H., Hatchell, J., Johnstone D., et al. 2018, ApJS, 238, 8 SOF 07-0147 issued by USRA to Northwestern University. E.G. C.-L., Liu, H. B., Lai, S.-P.,et al. 2020, ApJ, 889, 172 Kristensen, L. E., Klaassen, P. D., Mottram, J. C., Schmalzl, M., & acknowledgesupportfrom the National ScienceFoundation through the NSF MPS Ascend Fellowship grando. 2213275. Ladjelate, B., André, P., Könyves, V., et al. 2020, A&A, 638, A74 K.P. is a Royal Society University Research Fellow, supported lby arian, A. 2007, JQSRT, 106, 225 Le Gouellec, V. J. M., Hull, C. L. H., Maury, A. J., et al. 2019, ApJ, 885, 106 grant No. URF□R1□21132/2/e thank Naomi Hirano for Lee, A. T., Offner, S. S. R., Kratter, K. M., Smullen, R. A., & Li, P. S. 2019, providing us with the calibrated SMA CO observations in Figure 5. We thank John Tobin for discussions on binarity and Zhi-Yun Li for discussions magnetic field alignment with column densityThis paper makes use of the following ALMA data: ADS/JAO.ALMA#2015.1.01112.S. ALMA is a partnershipLynds, B. T. 1962, ApJS, 7, 1 of ESO (representing its member states), NSF (USA), and NINByo, A. R., Kim, J., Sadavoy, S., et al. 2021, ApJ, 918, 85 (Japan), together with NPC (Canada), NSTC and ASIAA Maureira, M. J., Pineda, J. E., Segura-CoxD. M., et al. 2020, ApJ, 897, 59 (Japan), together with NRC (Canada), NSTC and ASIAA (Taiwan), and KASI (Republic of Korea), in cooperation with the Republic of Chile. The Joint ALMA Observatory is operated Instrument Handbook/ersion 3 (Pasaden & A: SSC). by ESO, AUI/NRAO, and NAOJ. The National Radio Astronom Mizuno, A., Fukui, Y., Iwata, T., Nozawa, S., & Takano, T. 1990, ApJ, Observatory isa facility of the National Science Foundation operated under cooperative agreement by Associated Universities, M., & Kratter, K. M. 2018, ApJ, 854, 44 Inc.

ORCID iDs

Frankie J.Encalada https://orcid.org/0000-0002-3566-6270 Leslie W. Looney https://orcid.org/0000-0002-4540-6587 Giles Novak® https://orcid.org/0000-0003-1288-2656 Sarah Sadavov https://orcid.org/0000-0001-7474-6874 Erin G. Cox https://orcid.org/0000-0002-5216-8062 Fabio Pereira-Santoshttps://orcid.org/0000-0002-9650-3619 Dennis Lee https://orcid.org/0000-0002-3455-1826 Rachel Harrison https://orcid.org/0000-0003-2118-4999 Kate Pattle® https://orcid.org/0000-0002-8557-3582

References

```
Chapman, N. L., Davidson, J. A., Goldsmith, P. F., et al. 2013, ApJ, 770, 151
Chen, C.-Y., King, P. K., & Li, Z.-Y. 2016, ApJ, 829, 84
Chuss, D. T., Andersson B. G., Bally, J., et al. 2019, ApJ, 872, 187
Clarke, M., Perera, D., Berthoud, M., et al. 2020, HAWC+ DRP User's
   Manual, v3.2.0, Github, https://sofia-usra.github.io/sofia_redux/manuals/
   hawc/users/users.html
Cox, E. G., Harris, R. J., Looney, L. W., et al. 2018, ApJ, 855, 92
Cox, E. G., Novak, G., Sadavoy, S. I., et al. 2022, ApJ, 932, 34
Crimier, N., Ceccarelli, C., Maret, S., et al. 2010, A&A, 519, A65
Dowell, C. D. 1997, ApJ, 487, 237
Dzib, S. A., Ortiz-León, G. N., Hernández-Gómez, et al. 2018, A&A,
   614, A20
Encalada F. J., Looney, L. W., Tobin, J. J., et al. 2021, ApJ, 913, 149
Fukui, Y., Sugitani, K., Takaba, H., et al. 1986, ApJL, 311, L85
Galametz, M., Maury, A., Girart, J. M., et al. 2018, A&A, 616, A139
Girart, J. M., Estalella, R., Palau, A., Torrelles, J. M., & Rao, R. 2014, ApJL,
   780, L11
Harper, D. A., Runyan, M. C., Dowell, C. D., et al. 2018, JAI, 07, 1840008
Harris, R. J., Cox, E. G., Looney, L. W., et al. 2018, ApJ, 861, 91
Hildebrand, R. H., Davidson, J. A., Dotson, J. L., et al. 2000, PASP, 112, 1215 Vrba, F. J., Strom, S. E., & Strom, K. M. 1976, AJ, 81, 958
Houde, M., & Vaillancourt, J. E. 2007, PA
Huang,B., Girart, J. M., Stephensl. W., et al. 2024, ApJL, 963, L31 Hull, C. L. H., Girart, J. M., & Tychoniec, Ł. 2017, ApJ, 847, 92
Hull, C. L. H., Le Gouellec, V. J. M., Girart, J. M., Tobin, J. J., & Bourke, T. L.
   2020, ApJ, 892, 152
Hull, C. L. H., Plambeck, R. L., Kwon, W., et al. 2014, ApJS, 213, 13
JacobsenS. K., JørgensenJ. K., van der Wiel, M. H. D., et al. 2018, A&A,
   612, A72
Jørgensen J. K., van der Wiel, M. H. D., Coutens, A., et al. 2016, A&A,
   595, A117
```

```
pJ, 887, 232
Lee, D., Berthoud, M., Chen, C.-Y., et al. 2021, ApJ, 918, 39
Liu, H. B. 2021, ApJ, 914, 25
Looney, L. W., Mundy, L. G., & Welch, W. J. 2000, ApJ, 529, 477
Maury, A. J., Girart, J. M., Zhang, Q., et al. 2018, MNRAS, 477, 2760
MIPS Instrument And MIPS Instrument Support Teams 2011, MIPS
   356, 184
Novak, G. 2011, in ASP Conf. Ser. 449, Astronomical Polarimetry 2008:
   Science from Small to Large Telescopesed. P. Bastien et al. (San
   Francisco,CA: ASP), 50
Novak, G., Dotson, J. L., Dowell, C. D., et al. 1997, ApJ, 487, 320
Padoan, P., & Nordlund, A. 2002, ApJ, 576, 870
Pattle, K., Fissel, L., Tahani, M., Liu, T., & Ntormousi, E. 2023, in ASP Conf.
   Ser. 534, Protostars and Planets Vettl, S.-i. Inutsuka et al. (San Francisco,
   CA: ASP), 193
Pattle, K., Lai, S.-P., Di Francesco J., et al. 2021, ApJ, 907, 88
Pattle, K., Lai, S.-P., Sadavoy, S., et al. 2022, MNRAS, 515, 1026
Pattle, K., Ward-Thompson, D., et al. 2017, ApJ, 846, 122
Pattle, K., Ward-Thompson, D., Kirk, J. M., et al. 2015, MNRAS, 450, 1094
Pineda, J. E., Maury, A. J., Fuller, G. A., et al. 2012, A&A, 544, L7
Planck Collaboration, Ade, P. A. R., Aghanim, N., et al. 2016, A&A,
   586 A138
Adams, F. C., Ruden, S. P., & Shu, F. H. 1989, ApJ, 347, 959
Rao, R., Girart, J. M., Marrone, D. P., Lai, S.-P., & Schnee, S. 2009, ApJ,
Rodríguez, L. F., Loinard, L., D'Alessio, P., Wilner, D. J., & Ho, P. T. P. 2005,
   ApJL, 621, L133
Sadavoy, S. I., Myers, P. C., Stephensl. W., et al. 2018, ApJ, 869, 115
Sadavoy, S. I., Stephensl. W., Myers, P. C., et al. 2019, ApJS, 245, 2
Sánchez-PortaM., Marston,A., et al. 2014, ExA, 37, 453
Scarrott, S. M., & Warren-Smith, R. F. 1989, MNRAS, 237, 995
Schöier, F. L., Jørgensen J. K., van Dishoeck, E. F., & Blake, G. A. 2002,
       , 390, 1001
Stark, R., Sandell, G., Beck, S. C., et al. 2004, ApJ, 608, 341
Stephensl. W., Myers, P. C., Zucker, C., et al. 2022, ApJL, 926, L6
Tobin, J. J., Looney, L. W., Li, Z.-Y., et al. 2016, ApJ, 818, 73
Tobin, J. J., Offner, S. S. R., Kratter, K. M., et al. 2022, ApJ, 925, 39
Tsukamoto, Y., Maury, A., Commercon, B., et al. 2023, in ASP Conf. Ser. 534,
   Protostars and Planets VIIed. S.-i. Inutsuka et al. (San Francisco,CA:
   ASP), 317
Vaillancourt, J. E., Chuss, D. T., Crutcher, R. M., et al. 2007, Proc. 6678,
   66780D
van der Wiel, M. H. D., Jacobsen, S. K., Jørgensen, J. K., et al. 2019, A&A,
   626, A93
Walker, C. K., Lada, C. J., Young, E. T., & Margulis, M. 1988, ApJ, 332, 335
Wootten, A. 1989, ApJ, 337, 858
Wootten, A., & Loren, R. B. 1987, ApJ, 317, 220
Wright, E. L., Eisenhardt, P. R. M., Mainzer, A. K., et al. 2010, AJ,
   140, 1868
Yang, H., Li, Z.-Y., Looney, L., & Stephens, J. 2016, MNRAS, 456, 2794
Yeh, S. C. C., Hirano, N., Bourke, T. L., et al. 2008, ApJ, 675, 454
Zamponi, J., Maureira, M. J., Zhao, B., et al. 2021, MNRAS, 508, 2583
Zhang, Q., Qiu, K., Girart, J. M., et al. 2014, ApJ, 792, 116
Zielinski, N., Wolf, S., & Brunngräber, R. 2021, A&A, 645, A125
```

Hogerheijde, M. R. 2013, A&A, 549, L6